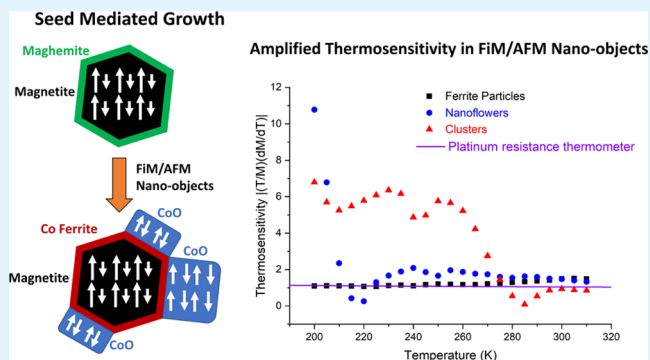


# Thermosensitivity through Exchange Coupling in Ferrimagnetic/Antiferromagnetic Nano-Objects for Magnetic-Based Thermometry

Frank M. Abel,\* Eduardo L. Correa, Adam J. Biacchi, Think Q. Bui, Solomon I. Woods, Angela R. Hight Walker, and Cindi L. Dennis

**ABSTRACT:** Temperature is a fundamental physical quantity important to the physical and biological sciences. Measurement of temperature within an optically inaccessible three-dimensional (3D) volume at microscale resolution is currently limited. Thermal magnetic particle imaging (T-MPI), a temperature variant of magnetic particle imaging (MPI), hopes to solve this deficiency. For this thermometry technique, magnetic nano-objects (MNOs) with strong temperature-dependent magnetization (thermosensitivity) around the temperature of interest are required; here, we focus between 200 K and 310 K. We demonstrate that thermosensitivity can be amplified in MNOs consisting of ferrimagnetic (FiM) iron oxide (ferrite) and antiferromagnetic (AFM) cobalt oxide (CoO) through interface effects. The FiM/AFM MNOs are characterized by X-ray diffraction (XRD), (scanning) transmission electron microscopy (STEM/TEM), dynamic light scattering (DLS), and Raman spectroscopy. Thermosensitivity is evaluated and quantified by temperature-dependent magnetic measurements. The FiM/AFM exchange coupling is confirmed by field-cooled (FC) hysteresis loops measured at 100 K. Magnetic particle spectroscopy (MPS) measurements were performed at room temperature to evaluate the MNOs MPI response. This initial study shows that FiM/AFM interfacial magnetic coupling is a viable method to increase thermosensitivity in MNOs for T-MPI.

**KEYWORDS:** magnetic nano-objects, FiM/AFM exchange coupling, colloidal synthesis, thermal magnetic particle imaging, thermosensitivity



## INTRODUCTION

Measurement of temperature is critical to every scientific discipline. As technology advances, thermometry with spatial resolution becomes crucial to fully develop applications in the areas of biomedicine,<sup>1</sup> integrated photonic devices,<sup>2</sup> fuel cells,<sup>3</sup> combustion engines,<sup>4</sup> microelectronics,<sup>5</sup> and additive manufacturing,<sup>6,7</sup> to name a few. Remote thermometry, within an optically opaque 3D volume, with microscale resolution, is generally not possible. Thermal magnetic particle imaging (T-MPI),<sup>8</sup> which is based on the nonlinear magnetic response of magnetic nano-objects (MNOs), is currently at the forefront of possible solutions. However, T-MPI requires MNOs that exhibit strong temperature-dependent magnetization (thermosensitivity) near room temperature (200 K to 400 K). Commercially produced colloidal nanoparticles typically show minimal change in magnetization with temperature in this temperature range. Here, we focus on the development of MNOs with good thermosensitivity around room temperature.

Core-shell and bimagnetic nano-objects of ferromagnetic/ferrimagnetic (F(i)M) and AFM materials have been previously studied due to their potential to exhibit exchange bias (EB). EB is an interfacial coupling effect between the

F(i)M and AFM, which can lead to changes in the coercivity of the MNOs. These effects have been studied in Co/CoO formed by controlled oxidation;<sup>9–13</sup>  $\text{Fe}_{3-d}\text{O}_4/\text{CoO}$ <sup>14–17</sup> and  $\text{CoFe}_2\text{O}_3/\text{CoO}$ <sup>18</sup> produced by seed-mediated growth; and  $\text{FeO}/\text{Fe}_3\text{O}_4$ ,<sup>19–22</sup>  $\text{MnO}/\text{Mn}_3\text{O}_4$ ,<sup>23</sup>  $\text{CoO}/\text{Fe}_3\text{O}_4$ ,<sup>24</sup>  $\text{CoO}/\text{CoFe}_2\text{O}_4$ ,<sup>25</sup>  $\text{CoO}/\text{Co}_{1-x}\text{Zn}_x\text{Fe}_2\text{O}_4$ ,<sup>26</sup> and  $\text{Co}_y\text{Fe}_{1-y}\text{O}/\text{Co}_x\text{Fe}_{3-x}\text{O}_4$ <sup>27</sup> synthesized by a variety of colloidal methodologies. Despite some fundamental studies on these materials, no new technologies have emerged to utilize this type of exchange coupling in MNOs. Recent computational work has suggested that in core-shell nanoparticles of ferromagnetic iron and gadolinium with antiferromagnetic interfacial exchange coupling, a sharp change in the magnetization with temperature can occur.<sup>28</sup> This temperature feature shows

tunability, with the core radius and core/shell thickness ratio as independent parameters.

We synthesized ferrite/CoO MNOs by a seed-mediated colloidal growth approach. The FiM/AFM MNOs were physically characterized by X-ray diffraction (XRD), dynamic light scattering (DLS), Raman spectroscopy, and (scanning) transmission electron microscopy (STEM/TEM). The magnetic and thermal properties of the MNOs were characterized by direct current (DC) and alternating current (AC) magnetometry measurements as a function of temperature plus room-temperature magnetic particle spectroscopy (MPS). The results show the proof-of-concept of amplified thermo-sensitivity through interface effects.

## ■ SIZE AND STRUCTURAL CHARACTERIZATION

The MNOs produced in this work were synthesized by a seed-mediated colloidal growth approach. Ferrite particles were first synthesized and used as seeds to grow the antiferromagnetic CoO in a second synthesis step. Details are given in the [Material Synthesis and Characterization Methods](#) section. Crystal structures, *d*-spacing, lattice parameters, crystallite sizes, and qualitative phase quantities were evaluated by powder XRD, as shown in [Figure 1](#). The ferrite MNOs were

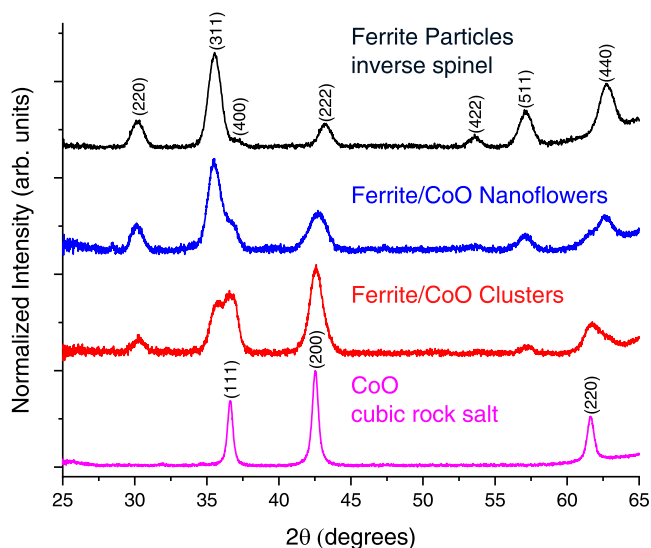


**Figure 1.** XRD of the representative ferrite seed material indexed to the inverse spinel structure, ferrite/CoO nanoflowers with majority ferrite phase, ferrite/CoO clusters with majority CoO phase, and CoO indexed to the cubic rock salt structure. The background has been subtracted from the data.

indexed to the inverse spinel structure and the CoO MNOs were indexed to the cubic rock salt structure. All ferrite/CoO samples show both the inverse spinel and cubic rock salt structures, but the relative peak intensity differs according to the synthesis conditions. One sample (using 48 mg ferrite particles) has a majority inverse spinel ferrite phase, showing the (311) peak with the highest intensity, and is labeled as nanoflowers. The other (using 32 mg ferrite particles) has a majority of CoO cubic rock salt phase, showing the (200) peak with the highest intensity, and is labeled as clusters. The lattice parameters of the ferrite particles were determined to be approximately 0.837 nm compared to the ferrite phase in the nanoflowers and clusters of about 0.838 and 0.837 nm, respectively, determined from the (311) peak. Comparing the

lattice parameter of CoO, approximately 0.425 nm, with the CoO phase in the nanoflowers with a lattice parameter of about 0.424 nm and 0.425 nm for the clusters, a similarly small difference is observed, determined from the (111) peak. The minimal changes in lattice parameters between the nanoflowers and clusters to that of the reference ferrites and CoO suggest minimal diffusion of Co into ferrites. However, XRD is not reliable in differentiating ferrite from Co ferrite due to the small difference in atomic size between Co and Fe atoms. Interface diffusion will be investigated in more detail by Raman spectroscopy and STEM further in the text. The crystallite sizes were estimated based on the broadening of the (311) peak for the ferrite phases, with the ferrite particles and the nanoflowers and clusters all having an approximate size of 8 nm. Alternatively, CoO synthesized without ferrite particles has a crystallite size of approximately 19 nm compared to 9 nm for the nanoflowers and clusters estimated from the (111) peak. The significant change in crystallite size due to the presence of the ferrite particles suggests that they affect the nucleation and growth of the CoO phase, leading to interfaced materials, as will be observed in the TEM data. [Table S1](#) summarizes synthesis details including the morphology and the corresponding quantity of ferrite seeds, precursors, crystallite sizes, TEM size, and DLS size when available.

The size, morphology, and interface between the crystal structures were investigated by TEM. [Figure 2a](#) is a TEM image of the ferrite particles with corresponding size distributions from TEM and DLS. The mean size determined from TEM is 10 nm with a standard deviation of 2 nm. The mean hydrodynamic size is approximately 12 nm (main peak). The nanoflower sample with majority ferrite phase is composed of irregular shaped particle-like objects with a mean cross section of 13 nm and standard deviation of 3 nm ([Figure 2b](#)). The mean hydrodynamic size from DLS was found to be approximately 22 nm. The difference between the TEM size and DLS size is most likely due to a combination of the organic surfactants on the surface and the nonspherical nature of the nanoflowers leading to additional errors in size estimation by DLS. The cluster sample with the majority of the CoO phase shows tightly packed polycrystalline objects ([Figure 2c](#)). In this case, the mean hydrodynamic size was found to be approximately 74 nm, suggesting that these objects remain intact when dispersed in hexanes.

The next step is to examine the interface between the ferrite and CoO using high-resolution (HR)-TEM. [Figure 2d](#) shows HR-TEM of a single ferrite particle. The *d*-spacing of this particle was determined by averaging across the line indicated by arrows and was found to be approximately 0.254 nm; a similar value of 0.2523 nm was determined from XRD for the (311) plane of the inverse spinel structure. In [Figure 2e](#), the nanoflower sample is shown, which has clear crystalline interfaces between the ferrite center with the (311) plane and the cubic rock salt CoO phase identified by the (111) plane. In this case, it appears as if CoO forms an interface with the ferrite and grows from the faceted sides of the particle. The *d*-spacing of about 0.253 nm for the (311) plane determined from HR-TEM agrees with the value determined by XRD of 0.2526 nm; likewise, the *d*-spacing values of approximately 0.242 nm and 0.243 nm for the (111) CoO plane are close to the value of 0.2447 nm from XRD measurements. The cluster sample shows a similar ferrite center with CoO growing from the surface of the particle, creating a crystalline interface between the two phases ([Figure 2f](#)). A *d*-spacing value of about

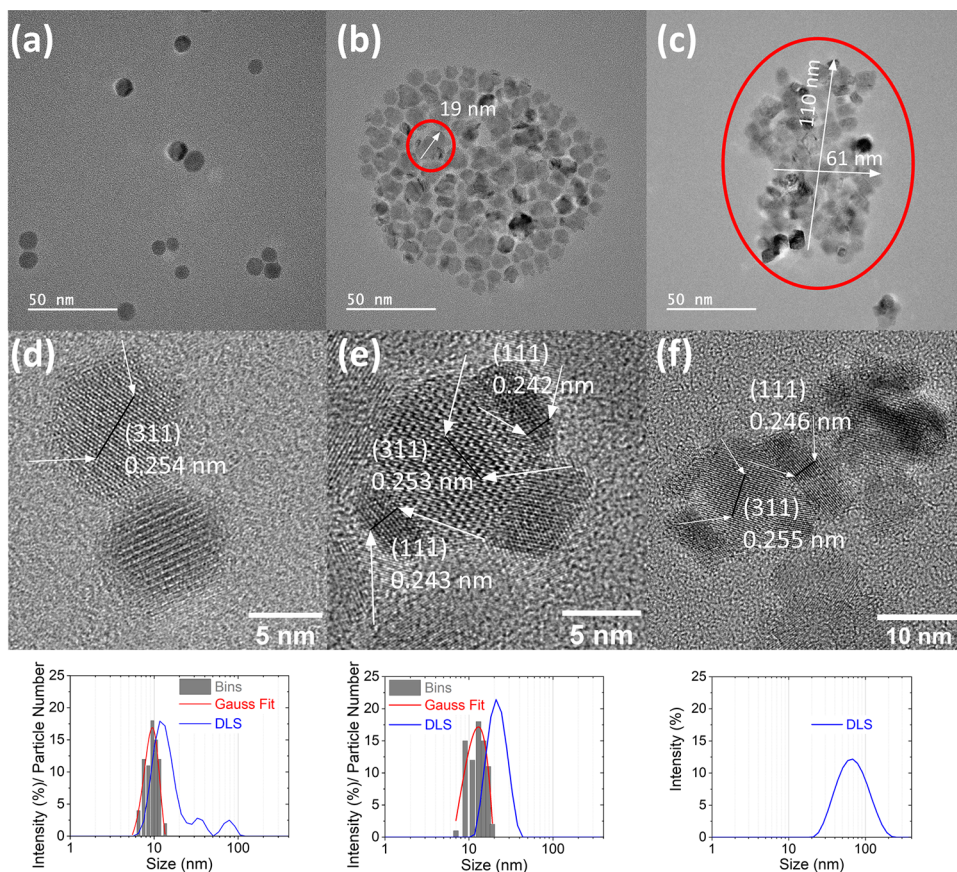


**Figure 2.** TEM images and corresponding size distributions determined from TEM and DLS of ferrite particles (a, d), ferrite/CoO nanoflowers (b, e), and ferrite/CoO clusters (c, f). The large (>100 nm) object observed in the TEM image of the nanoflowers is most likely a drying artifact from sample preparation. Values for TEM and DLS size were rounded to whole numbers. Red circles with arrows indicate the length measured and show the approximate objects that remain intact when dispersed in hexanes. In the high-resolution TEM images, the *d*-spacings were determined by averaging over the line indicated by the sets of two arrows. The crystal planes are labeled.

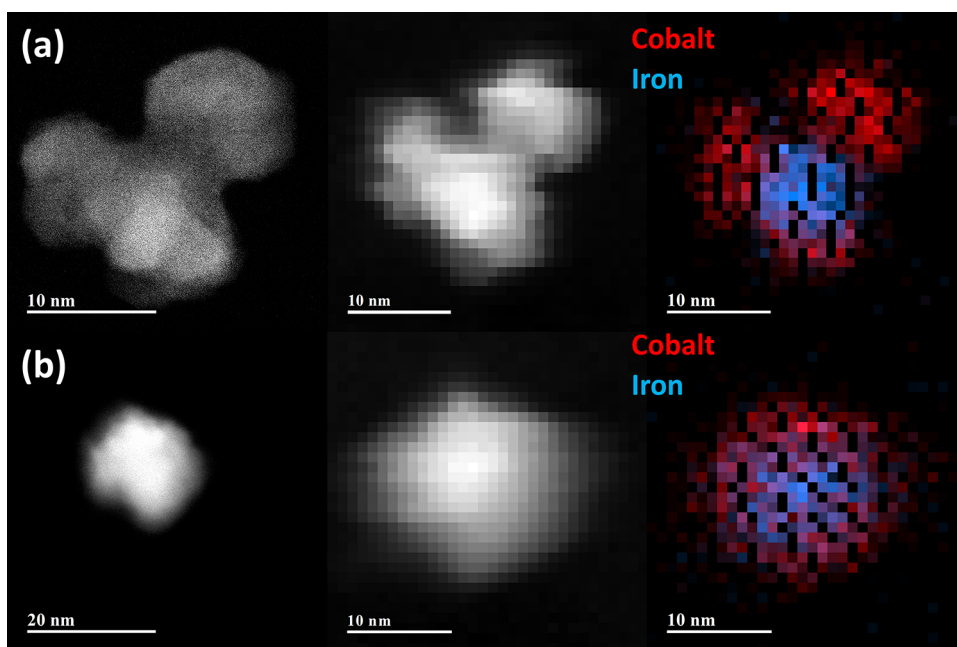


**Figure 3.** STEM image, the STEM image generated with mapping, and the superposition of cobalt (red) and iron (blue) elemental mapping of the nanoflower sample showing an irregularly shaped particle (a) and a more spherical particle (b).

0.255 nm was found for the (311) plane of the ferrite compared to 0.2522 nm determined from XRD; for the (111) plane of CoO, the value of approximately 0.246 nm is in similar agreement with the XRD value of 0.2452 nm.

To further elucidate what is occurring at the interface after the growth of CoO on the ferrite particles, high-angle annular dark-field (HAADF) scanning transmission electron microscopy (STEM) imaging, energy-dispersive X-ray spectroscopy (EDXS) elemental mapping, and Raman spectroscopy were performed. Figure 3 shows STEM images and corresponding elemental maps of representative morphologies in the ferrite/CoO nanoflower sample. In Figure 3a, cobalt-rich protuberances are shown growing from the iron-rich ferrite center. This image closely matches the particle shown in HR-TEM image in Figure 2e, with these cobalt regions being identified as the cubic rock salt structure of CoO and the iron-rich region having the inverse spinel structure. Figure 3b shows a more spherical particle that has a cobalt-rich surface with a similar iron-rich core. At the interface, there appears to be diffusion between the cobalt- and iron-rich regions. Line scans of these particles in Figure S1 reveal a relatively uniform signal of cobalt coming from the iron-rich cores, with the largest protuberance in the irregular particle and the surface of the more spherical particle being nearly all cobalt. An additional STEM image and elemental map of another particle from the nanoflower sample is shown in Figure S2 with similar features. The STEM elemental mapping results suggest cobalt may diffuse into the ferrite particles, followed by the growth of the CoO phase. Alternatively, the cobalt signal coming from the iron-rich regions may simply reside on the surface of the particles.

Raman spectroscopy in Figure 4 was used to identify structural features not detectable by XRD. Figure 4 shows Raman spectra of representative ferrite particles, nanoflowers, clusters, and CoO. The ferrite particles have two primary modes at  $664\text{ cm}^{-1}$  and  $701\text{ cm}^{-1}$ . These can be identified as the  $A_{1g}$  modes of magnetite and maghemite; the values are in relatively good agreement with what has been reported in iron oxide thin films,<sup>29</sup> and in previous work including both computational and experimental data.<sup>30</sup> The highest-intensity mode in the CoO spectra is at  $529\text{ cm}^{-1}$ . Previous reports on single-crystal samples<sup>31,32</sup> have identified a one-phonon longitudinal optical (LO) mode in the range of approximately  $540\text{ cm}^{-1}$  to  $560\text{ cm}^{-1}$  by reflectivity measurements,<sup>33</sup> but in a nanocrystalline sample with a cubic rock salt structure, a value of  $530\text{ cm}^{-1}$  has been reported, for this mode,<sup>33</sup> in close agreement with our findings.

In the nanoflower sample, two primary peaks can be identified at  $667\text{ cm}^{-1}$  and  $534\text{ cm}^{-1}$ ; in the clusters, these peaks are found at  $666\text{ cm}^{-1}$  and  $537\text{ cm}^{-1}$ . The peaks at  $666\text{ cm}^{-1}$  and  $667\text{ cm}^{-1}$  are the highest intensity mode of the ferrite and the peaks at  $534\text{ cm}^{-1}$  and  $537\text{ cm}^{-1}$  are that of CoO. Comparing these spectra to the spectra of ferrite particles, the most striking feature is the clear disappearance of the  $A_{1g}$  maghemite shoulder on the main  $A_{1g}$  magnetite peak. Additionally, the mode at  $368\text{ cm}^{-1}$ ,  $T_g$ , is no longer present, which also belongs to the maghemite phase. Maghemite typically exists on the surface of ferrite particles in a magnetite–maghemite core–shell or  $\text{Fe}_3\text{O}_4\text{--Fe}_{3-x}\text{O}_4$  configuration,<sup>34,35</sup> and the disappearance of these peaks after the growth of CoO strongly supports Co diffusion into the surface of the ferrite particles leading to the formation of a Co ferrite phase. Therefore, the shifts in these peaks may be related to

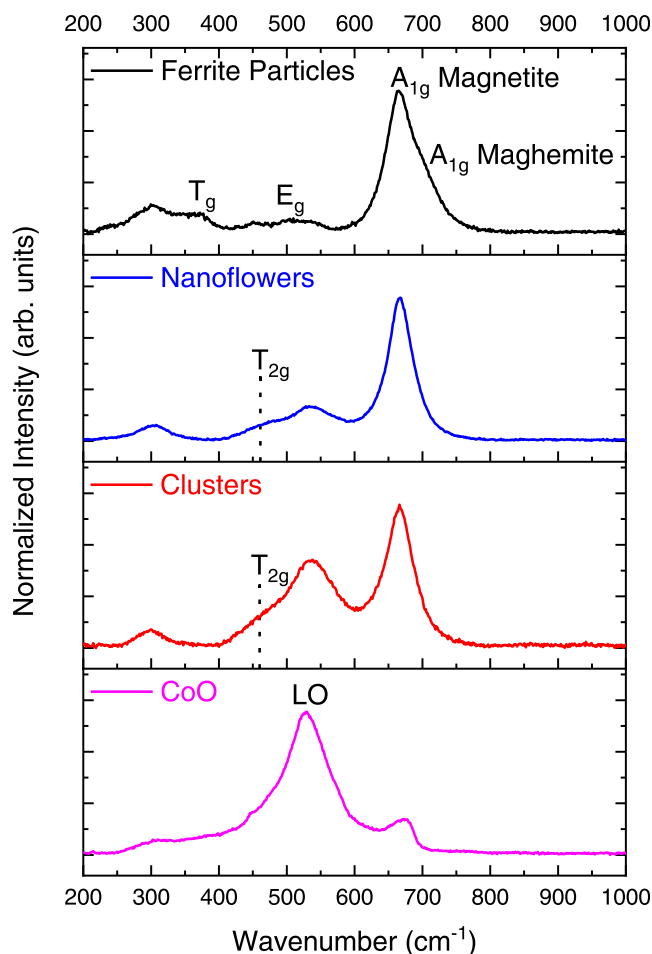


**Figure 4.** Raman spectra measured at an excitation wavelength of 785 nm and focused power of 3.8 mW of representative ferrite particles (black), ferrite/CoO nanoflowers (blue), ferrite/CoO clusters (red), and CoO (pink). The background has been subtracted from the data and normalized between 0 and 1.

diffusion at the interface leading to the formation of a lightly doped Co ferrite phase.

At lower wavenumbers, two additional modes are observed in the nanoflowers,  $302\text{ cm}^{-1}$  and  $461\text{ cm}^{-1}$ , and in the clusters,  $300\text{ cm}^{-1}$  and  $460\text{ cm}^{-1}$ . These modes are similar to those reported in Co ferrites.<sup>36,37</sup> The modes at  $460\text{ cm}^{-1}$  and  $461\text{ cm}^{-1}$ , labeled  $T_{2g}$  and with dotted lines, are the most distinct to the Co ferrite phase, and it can be observed that all four spectra clearly have modes in the range of  $300\text{ cm}^{-1}$  to  $307\text{ cm}^{-1}$ . Comparing the  $460\text{ cm}^{-1}/461\text{ cm}^{-1}$  modes to the CoO spectra, there is a similar shoulder on the main mode of CoO; however, the fitting of the spectra produced a value of  $447\text{ cm}^{-1}$ . To ensure this value was outside of experimental uncertainties, three measurements were performed on the nanoflower sample yielding a mean and standard deviation of this mode to be  $466\text{ cm}^{-1} \pm 5\text{ cm}^{-1}$ , suggesting this is a different mode not coming from the CoO phase. Lastly, compared to the ferrite spectra, a mode is identified at  $491\text{ cm}^{-1}$ ; however, the fit is poor due to the low intensity and broadness, but this most closely matches the  $E_g$  mode of maghemite.<sup>29,30</sup> As a note, the fitting of this peak in the ferrite spectra may also include the  $T_g$  peak of magnetite, which is near  $540\text{ cm}^{-1}$ .<sup>29,30</sup> Since we have already concluded that the maghemite phase is no longer present in the nanoflowers and

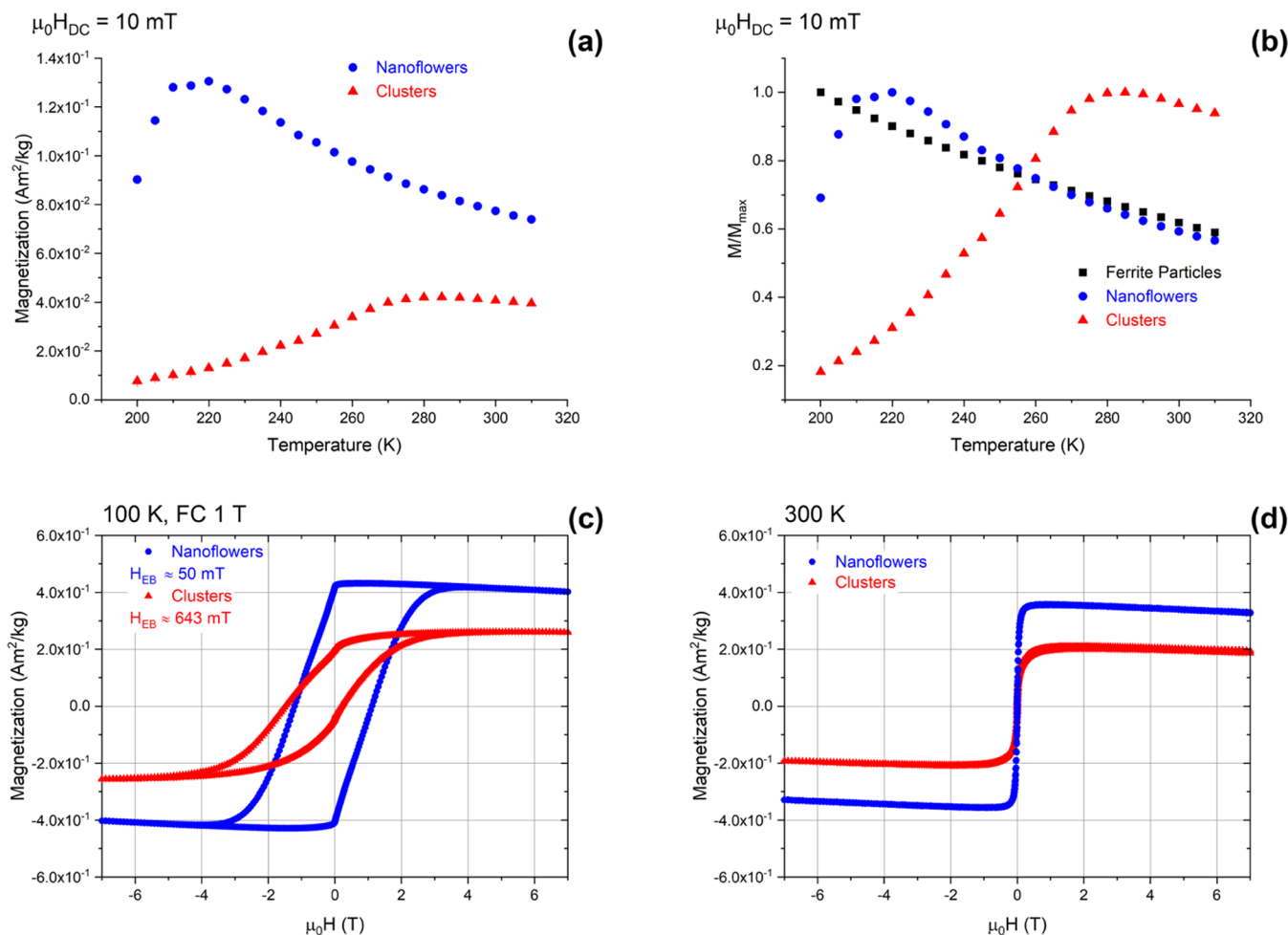


**Figure 5.** ZFC magnetization vs. temperature measured in a DC field of 10 mT (a), ZFC measurements normalized by the maximum magnetization between 200 K and 310 K (b), exchange bias magnetization vs. field hysteresis loops measured at 100 K after cooling in a DC field of 1 T (c), and magnetization vs. field hysteresis loops measured at 300 K (d). All samples were colloids, with the particles dispersed in hexanes, and are in a liquid state between 200 K and 310 K and frozen solid at 100 K. The nanoflowers and clusters had an approximate concentration of 10 mg/mL; the ferrite sample had an approximate concentration of 20 mg/mL. Error bars are shown for panels (a,c,d) but are smaller than the data point.

clusters, the mode at  $460\text{ cm}^{-1}/461\text{ cm}^{-1}$  gives further support to the formation of a Co ferrite phase. Fittings of the Raman spectra are presented in Figure S3.

Based on the Raman spectra and STEM elemental mapping, the following model is proposed. Co diffuses into the surface layer of the ferrite particles, followed by growth of the CoO phase, leaving nano-objects with three distinct phases: CoO, a Co-doped ferrite region/layer, and a magnetite core. The Raman spectra support the formation of a lightly doped Co ferrite due to the disappearance of the maghemite modes and the presence of a low-intensity mode near  $460\text{ cm}^{-1}$ . STEM mapping shows that the core remains iron-rich, and we can conclude that the center of the particles is most likely still magnetite.

## ■ MAGNETIC CHARACTERIZATION

Zero-field-cooled (ZFC) temperature-dependent magnetization measurements and temperature-dependent AC susceptibility (ACS) were used to investigate the thermosensitivity of the MNOs. The magnetometry measurements presented in the main text were all performed on samples in solution (hexanes), as our initial interest is to study materials for T-MPI in their colloidal state. The ZFC measurements of liquid samples

(hexanes) of the nanoflowers and clusters are shown in Figure 5a. The samples have an approximate concentration of 10 mg/mL and are normalized by the total mass of the samples, both solid material and solvent. The magnetization of the clusters increases with increasing temperature in the range of 200 K to 285 K. In contrast, the nanoflower sample shows an entirely different behavior, with a sharp increase in magnetization between 200 K and 220 K and a decreasing trend from 220 K to 310 K. Due to a factor of two difference between the ferrite particles and nanoflowers/clusters concentration, the relative changes in magnetization with temperature for the nanoflowers and clusters were compared to the ferrites by normalizing by the maximum magnetization in the 200 K to 310 K temperature range (Figure 5b). The bare ferrite particles show a nearly linear drop in magnetization between 200 K and 310 K, compared to the sharper rise in magnetization over nearly the entire range for the clusters and a sharp change in magnetization at the low end of this range for the nanoflowers. The ZFC and field-cooled (FC) measurements normalized by the total sample mass of the ferrite particles, nanoflowers, and clusters are shown in Figure S4. Additional magnetic measurements of samples with Ni doping are shown in Figure

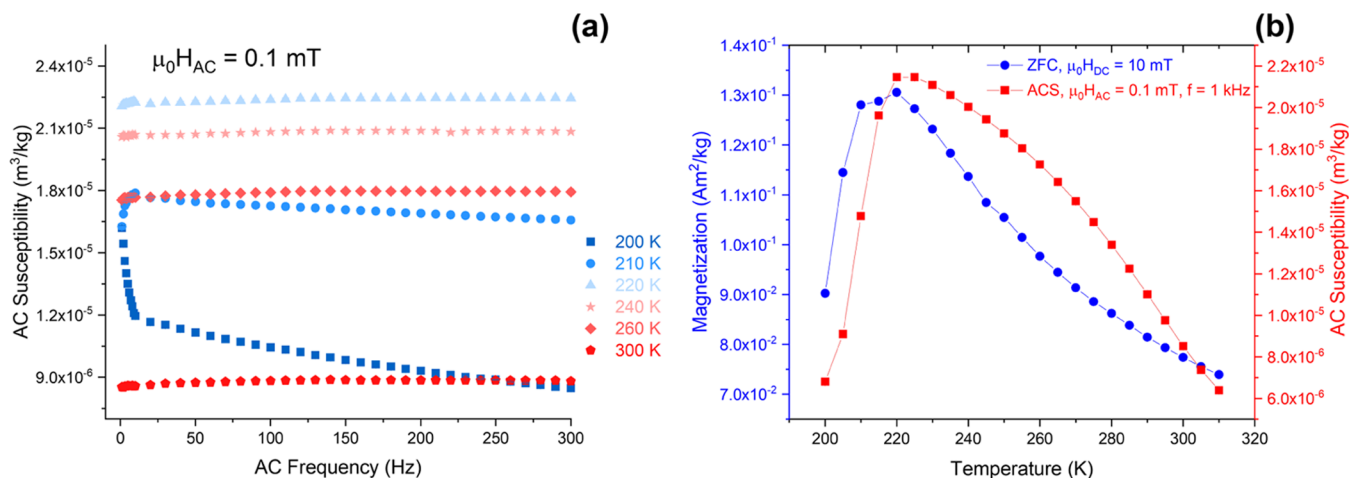


**Figure 6.** AC susceptibility of the colloidal nanoflowers at temperatures between 200 K and 300 K (a) and DC ZFC plotted alongside the ACS at 1 kHz as a function of the temperature of the nanoflowers (b). Error bars are shown but are smaller than the data point. The sample was measured in the colloidal state dispersed in hexanes.

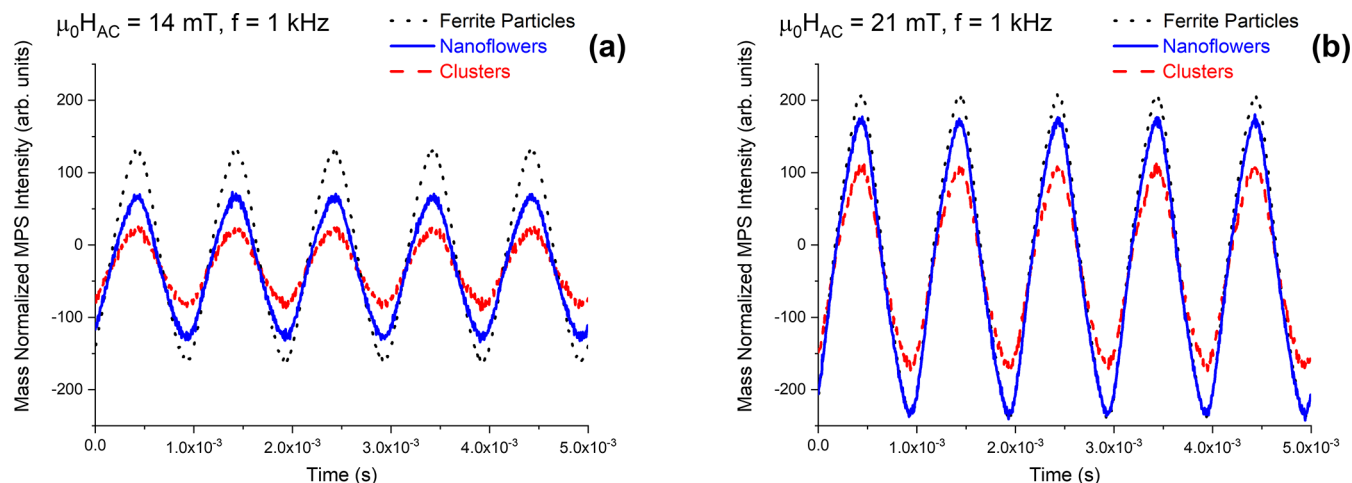


**Figure 7.** Room-temperature MPS measured at a drive peak amplitude of about 14 mT (10 mT RMS) and a frequency of 1 kHz (a) and a drive peak amplitude of about 21 mT (15 mT RMS) and a frequency of 1 kHz (b). The samples were colloids with the nanoparticles dispersed in hexanes and normalized by the mass of solid material in kilograms, estimated based on the approximate concentration of the samples.

**S5.** These samples have similar temperature-dependent magnetization behavior as the clusters.

To probe the exchange interactions between the FiM ferrite and AFM CoO, an exchange bias measurement was performed on the liquid samples. The samples were field-cooled in 1 T to 100 K, below the freezing point of hexanes, to immobilize the MNOs from physical rotation, after which a 7 T hysteresis loop was performed (Figure 5c). The nanoflowers show a square hysteresis loop with an exchange bias field of approximately 50 mT. It is likely that the particles form chains during the field cooling causing a cascading magnetic reversal resulting in the loop squareness. Alternatively, the clusters show a more rounded hysteresis suggesting less uniformity in the magnetic reversal. The clusters have an approximate exchange bias field of 643 mT. The difference in exchange bias is most likely related to the uniformity of coverage and thickness of antiferromagnetic CoO.<sup>10</sup> The highest exchange bias is measured for the sample with the largest amount of the CoO phase. The saturation magnetization is higher in the nanoflowers since it is majority ferrite phase compared to the clusters, which are majority CoO phase (Figure 5c,d).

To further investigate the temperature-dependent behavior of the nanoflowers, ACS measurements were performed between 200 K and 310 K. At 200 K, there is a sharp decrease in the ACS signal in the low-frequency range, suggesting that the drive field is not flipping the magnetization or energy is not entering the system (Figure 6a). At 210 K, there is an increase followed by a steady decrease with increasing frequency and between 220 K and 300 K, the ACS signal is nearly flat, suggesting a balance of energy in the system. Since the magnetocrystalline anisotropy is likely not changing significantly over the range of 200 K to 220 K, we think the change in the ACS signal is related to a change in the exchange bias field between the ferrite and CoO. Figure 6b shows the ACS at 1 kHz as a function of temperature, along with the DC ZFC measurement of the nanoflowers. The same trend is observed between the ACS and DC ZFC, and the sharp change in magnetization and susceptibility is most likely related to a reduction of the exchange coupling due to passing through the Néel temperature of CoO. The Néel temperature of bulk CoO is close to room temperature (289 K for a single-crystal sample);<sup>32</sup> however, in nanomaterials, finite size effects are known to reduce the antiferromagnetic to paramagnetic

transition. In CoO particles with sizes of 42 and 74 nm, values of 225 K and 280 K, respectively, have been reported.<sup>38</sup> These values are consistent with the observed maximum in the ZFC and ACS data of 220 K and 225 K for the nanoflowers.

Room-temperature liquid (hexanes) magnetic particle spectroscopy (MPS) measurements were performed to test the AC magnetic response of the MNOs under more realistic AC field conditions that will be used for T-MPI. Most notably, the AC drive field amplitudes are typically much higher than what is used in ACS. The chosen drive field amplitudes are in the range of typical values used in MPI. Figure 7 shows the MPS measurements at a frequency of 1 kHz with drive field peak amplitudes of approximately 14 mT (10 mT root mean square (RMS)), as shown in Figure 7a, and 21 mT (15 mT RMS), as shown in Figure 7b. The samples were normalized by the total mass of solid material in kilograms. At 14 mT (10 mT RMS), the MPS intensity seems to be proportional to the amount of ferrite in the nano-objects, with the nanoflower sample having a higher signal than the clusters. At the higher drive field peak amplitude of 21 mT (15 mT RMS), the MPS intensity of the nanoflower sample is comparable to that of the bare ferrite. With a drive field peak amplitude of 14 mT (10 mT RMS), the nanoflower MPS intensity was determined to be about 73% of the ferrite particles, and at 21 mT (15 mT RMS), the signal increased to about 93% of the ferrite particles MPS intensity. The Fourier transforms of the 21 mT, 1 kHz data are shown in Figure S6. Additionally, MPS measurements were performed at 7 kHz with a 14 mT (10 mT RMS) drive field peak amplitude, as shown in Figure S7, which shows an increase in the overall signal with improved signal-to-noise ratio.

### ■ THERMOSENSITIVITY OF MNOS

Thermosensitivity is a change in magnetization with temperature, but this needs to be defined more clearly to compare materials. Using the definition from thermometry,<sup>39,40</sup> but replacing the changing property of resistance with magnetization,<sup>41</sup> we get the following

$$S_M = \left| \left( \frac{T}{M(T)} \right) \left( \frac{dM(T)}{dT} \right) \right| \quad (1)$$

where  $M$  is magnetization and  $T$  is temperature. However, it is important to note that thermosensitivity is only one parameter that will affect the performance of a material for T-MPI. Thermosensitivity is also not the same as the temperature uncertainty obtained when the MNO is used in T-MPI, as the uncertainty must include the inherent noise in the measurement system itself.

Using eq 1, thermosensitivity curves as a function of temperature are calculated from the liquid DC ZFC measurements, shown in Figure 8. The thermosensitivity of the ferrite particles is nearly constant, being close to approximately 1 over the measured range. In contrast, thermosensitivity is greatly enhanced in some ranges of temperature in the FiM/AFM nano-objects. The nanoflowers show a large thermosensitivity of greater than 10 at 200 K, which rapidly decreases to be in line with the ferrite particles at higher temperatures. In the clusters, the mean thermosensitivity is approximately 6 between 200 K and 260 K, decreasing to about 1 at 275 K. The results show that thermosensitivity can be increased by interface effects and can be greatly affected by sample morphology (particle-like nanoflowers vs. clusters) in liquid samples.

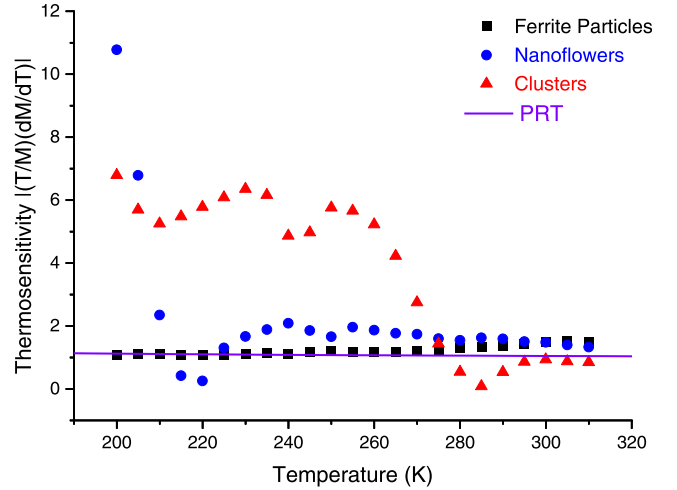


**Figure 8.** Thermosensitivity curves calculated from the DC ZFC measurements for the colloidal ferrite particles, nanoflowers, and clusters dispersed in hexanes. The thermosensitivity of a platinum resistance thermometer (PRT) is shown for comparison to the magnetic thermosensitivity of the nano-objects.

The observed enhancement in thermosensitivity in the nanoflowers and clusters compared to the bare ferrite particles can be directly related to exchange coupling between the ferrite and CoO and possibly due to changes in magnetic anisotropy due to Co diffusion into the ferrite. Both of these effects at low temperatures will increase the coercivity of the materials. As temperature increases, thermal energy allows the moments of the particles to be aligned more easily with the small applied field, increasing the magnetization and reducing the coercivity. More importantly, crossing the Néel temperature of the CoO results in sharp changes in magnetization with temperature. As shown in the ZFC data, this transition occurs over different temperature ranges between the nanoflowers and clusters. Specifically, the observed maximums in the ZFC data for the nanoflowers of 220 K and 285 K for the clusters agree well with reported values of the Néel temperature of CoO nanoparticles of different sizes.<sup>38</sup> These values are in excellent agreement with the transition from enhanced thermosensitivity to a thermosensitivity of about 1 (similar to the ferrite particles alone). While the nanoflowers and clusters studied here have similar sizes of individual crystals, they have widely varying amounts of surface contact between CoO and the ferrite, resulting in an enhancement of the exchange coupling in the clusters as compared to the nanoflowers. This means that the nanoflowers can see a significant loss of exchange coupling very rapidly near the Néel temperature of 220 K (as shown in Figure 8), while the clusters do not see it until a higher temperature of 285 K.

The enhanced thermosensitivity was only observed at lower temperatures and not around room temperature (300 K); Ni doping was considered, with the aim of increasing the Néel temperature of the CoO. However, as shown in the Supporting Information, we observed that these Ni-doped samples had similar sharp changes in magnetization in the ZFC data as the clusters without Ni. The maximum in the ZFC of the Ni-doped samples (Figure S5a,c) is nearly the same as that of the undoped clusters, at 280 K, 285 K, and 290 K for the three samples. We speculate the Ni preferentially enters the ferrite particles rather than the CoO or possibly sits at the interface. Raman spectroscopy showed that increasing the power

resulted in enhancement of the  $T_{2g}$  peak at  $464\text{ cm}^{-1}$  (Figure S3f), which did not occur at the same power for the samples without Ni. This suggests that Ni enters the ferrite structure as opposed to or in addition to CoO, which agrees with the minimal change in ZFC maximum, which we attribute to being related to the Néel temperature of the antiferromagnet.

To expand upon this initial study, two other potential solutions may exist which would allow for tunability of the thermosensitivity around and above room temperature. The first is to consider using already doped ferrites such as Zn, which would increase the magnetization and possibly result in the Ni entering the CoO as opposed to the core material. Alternatively, moving away from ferrite to magnetic transition metal alloys such as FeCo cores interfaced with CoO may also allow the doping of Ni into CoO. In addition to the consideration of new materials, we suspect that the sharp changes in magnetization observed in the DC ZFC measurements will shift to higher temperatures with high-frequency AC MPS measurements.

## CONCLUSIONS

We have demonstrated that thermosensitivity can be increased in FiM/AFM exchange coupled ferrite/CoO nano-objects produced through a seed-mediated colloidal synthesis approach. The observed changes after CoO growth in temperature-dependent magnetic measurements are most likely related to exchange coupling caused by the interface interactions between the FiM and AFM as well as Co diffusion into the surface of the ferrite particles.

We show that FiM/AFM MNOs can have comparable MPS intensities to the starting ferrite seed particles depending on the AC drive field amplitude. The thermosensitivity for MNO-based thermometry is defined and used to quantify the amplified thermosensitivity due to these interface effects in the synthesized MNOs. This initial study on creating thermosensitive MNOs through FiM/AFM exchange coupling lays a foundation for the further development of these MNO-based thermometers, which will enable the success of T-MPI.

## MATERIAL SYNTHESIS AND CHARACTERIZATION METHODS

**Synthesis of Ferrites Particles.** The ferrites were synthesized by thermal decomposition of iron(III) acetylacetonate,<sup>42,43</sup>  $\text{Fe}(\text{acac})_3$ , in a mixture of 9 mL of oleylamine (70%) and 1 mL of oleic acid.<sup>44</sup>  $\text{Fe}(\text{acac})_3$  was combined with the organic compounds at room temperature with a magnetic stir bar and put under vacuum, followed by the addition of an Ar blanket. Under continuous Ar flow and stirring at  $73.3\text{ rad/s}$ , the mixture was heated to approximately  $393\text{ K}$  (set point) for 30 min and heated to approximately  $573\text{ K}$  (set point) for 1 h. After cooling, the particles were precipitated with ethanol and separated by centrifugation. The particles were redistributed in hexanes and precipitated again with ethanol and then separated again by centrifugation before finally being dispersed in hexanes.

**Synthesis of CoO.** CoO was synthesized by thermal decomposition of cobalt(III) acetylacetonate,  $\text{Co}(\text{acac})_3$ , in 10 mL of oleylamine (70%). The  $\text{Co}(\text{acac})_3$  was combined at room temperature with the oleylamine using a magnetic stir bar, the temperature controller was set to  $393\text{ K}$ , and vacuum was pulled as the mixture was heated while stirring at  $73.3\text{ rad/s}$ . Vacuum was held at approximately  $393\text{ K}$  (set point) for about 15 min, followed by the addition of an Ar blanket. The mixture was then heated to approximately  $413\text{ K}$  (set point) for 20 min, followed by heating to approximately  $488\text{ K}$  (set point) for 1 h. Once cooled, the material was precipitated by the addition of ethanol and separated by centrifugation. The materials

were dispersed in hexanes for storage. The synthesis of CoO materials was adapted from the work of Shi and He.<sup>38</sup>

**Synthesis of Ferrite/CoO Nano-Objects.** The ferrite/CoO nano-objects were grown by adding the ferrite particles in a hexanes colloidal suspension to the mixture of  $\text{Co}(\text{acac})_3$  and oleylamine at room temperature. In detail, approximately 32 mg or 48 mg of ferrites in hexanes (mass values based on estimated concentrations) were added by micropipette to 1 mmol or 0.75 mmol of  $\text{Co}(\text{acac})_3$  in 10 mL of oleylamine (70%) while the mixture was continuously stirred at  $73.3\text{ rad/s}$  by a magnetic stir bar. The reaction vessel was sealed, and the temperature was set to  $393\text{ K}$  while vacuum was pulled. During heating, vacuum was carefully controlled as the hexanes began to boil off, and vacuum was maintained at approximately  $393\text{ K}$  (set point) for 15 min to ensure the hexanes were completely removed. The heating procedure was then performed in the same manner as the synthesis of the CoO synthesis. Once cooled, the material was precipitated by the addition of ethanol and separated by centrifugation and dispersed in hexanes for storage.

**Characterization of Magnetic Nano-Objects.** Powder X-ray diffraction (XRD) was performed with a Bruker D8 Discover X-ray diffractometer utilizing a  $\text{Cu K}\alpha$  radiation source. Bright-field TEM images were taken with an FEI Titan 80-300 at 300 kV. HAADF-STEM images and EDXS elemental maps were collected using a different FEI Titan 80-300 TEM operating at an accelerating voltage of 300 kV and equipped with an EDAX r-TEM spectrometer. For EDXS analysis of the data, K-shell transitions, which do not appreciably overlap, were chosen. Samples were drop-casted onto 300-mesh carbon-Formvar copper grids (Ted Pella). Dynamic light scattering (DLS) was measured using a Malvern Instruments Zetasizer Nano operated in backscatter mode at  $173^\circ$  with a 633 nm wavelength laser. The DLS was performed on dilute samples ( $\leq 0.1\text{ mg/mL}$ ) in hexanes. Raman spectra were collected on samples drop-casted on an Au-coated  $\text{Si/SiO}_2$  wafer using a Renishaw inVia system (1200 grooves/mm grating, 2.54 cm CCD detector) with a 785 nm excitation wavelength and at different powers as indicated. Liquid magnetic characterization was performed on a Superconducting Quantum Interference Device Vibrating-Sample Magnetometer (SQUID-VSM, Quantum Design). Liquid samples (about 70  $\mu\text{L}$ ) were mounted in LakeShore capsules and sealed using epoxy. The maximum applied field was 5.6 MA/m (70 000 Oe) for  $M$  vs.  $H$  and 8 kA/m (100 Oe) for  $M$  vs.  $T$  measurements. AC susceptibility was made using AC fields of 8 A/m (0.1 Oe) and 80 A/m (1 Oe) in a frequency range from 1 Hz to 1 kHz. For temperature-dependent AC susceptibility, the measurement temperature was changed from 200 K to 310 K. Magnetic particle spectroscopy (MPS) measurements were performed on a National Institute of Standards and Technology (NIST) built system and the drive field peak amplitudes were measured directly by a Hall probe for a given frequency, voltage, and amplifier gain. MPS was measured on samples in hexanes of approximately 1 mL volume in 2 mL capped vials. The estimation of nano-object concentrations is based on the total mass of dried materials for a given volume of the solvent.

## ASSOCIATED CONTENT

### Supporting Information

The Supporting Information is available free of charge at <https://pubs.acs.org/doi/10.1021/acsami.2c19673>.

Table summarizing the synthesis of various materials produced in this work, additional structural and magnetic characterization, including STEM elemental map line scans, additional STEM image and elemental map, fitting of Raman spectra, liquid ZFC and FC measurements, ZFC/FC, exchange bias of Ni-doped samples, Fourier transforms of MPS data, higher-frequency MPS data, and DC ZFC, and real part of the ACS of powder samples with a brief discussion (PDF)

## AUTHOR INFORMATION

### Corresponding Author

Frank M. Abel – National Institute of Standards and Technology (NIST), Gaithersburg, Maryland 20899, United States; [orcid.org/0000-0002-8828-7864](https://orcid.org/0000-0002-8828-7864);  
Email: [Frank.Abel@NIST.gov](mailto:Frank.Abel@NIST.gov)

### Authors

Eduardo L. Correa – National Institute of Standards and Technology (NIST), Gaithersburg, Maryland 20899, United States

Adam J. Bicchì – National Institute of Standards and Technology (NIST), Gaithersburg, Maryland 20899, United States; [orcid.org/0000-0001-5663-2048](https://orcid.org/0000-0001-5663-2048)

Thinh Q. Bui – National Institute of Standards and Technology (NIST), Gaithersburg, Maryland 20899, United States

Solomon I. Woods – National Institute of Standards and Technology (NIST), Gaithersburg, Maryland 20899, United States

Angela R. Hight Walker – National Institute of Standards and Technology (NIST), Gaithersburg, Maryland 20899, United States; [orcid.org/0000-0003-1385-0672](https://orcid.org/0000-0003-1385-0672)

Cindi L. Dennis – National Institute of Standards and Technology (NIST), Gaithersburg, Maryland 20899, United States

Complete contact information is available at:  
<https://pubs.acs.org/10.1021/acsami.2c19673>

### Funding

The authors thank the NIST's Innovations in Measurement Science: Thermal MagIC for project funding. The authors also thank Weston L. Tew for the discussion on thermosensitivity.

### Notes

We identify certain commercial equipment, instruments, or materials in this article to specify the experimental procedure adequately. In no case does such identification imply recommendation or endorsement by the National Institute of Standards and Technology, nor does it imply that the materials or equipment identified are necessarily the best available for the purpose.

The authors declare no competing financial interest.

## REFERENCES

- (1) Wang, S.; Westcott, S.; Westcott, S.; Chen, W. Nanoparticle Luminescence Thermometry. *J. Phys. Chem. B* **2002**, *106*, 11203–11209.
- (2) Savchuk, O. A.; Carvajal, J. J.; Pujol, M. C.; Massons, J.; Haro-González, P.; Martínez, O.; Jiménez, J.; Aguiló, M.; Díaz, F. New Strategies Involving Upconverting Nanoparticles for Determining Moderate Temperatures by Luminescence Thermometry. *J. Lumin.* **2016**, *169*, 711–716.
- (3) Lee, C.-Y.; Lee, S.-J.; Lo, Y.-M.; Liu, Y.-M. Micro Thermocouple and Voltage Sensor for Fuel Cell Real Time Interior Monitoring. *Int. J. Electrochem. Sci.* **2014**, *9*, 272–281.
- (4) Williams, B.; Edwards, M.; Stone, R.; Williams, J.; Edwart, P. High Precision In-Cylinder Gas Thermometry Using Laser Induced Grating: Quantitative Measurement of Evaporative Cooling with Gasoline/Alcohol Blends in a GDI Optical Engine. *Combust. Flame* **2014**, *161*, 270–279.
- (5) Brites, C. D. S.; Lima, P. P.; Silva, N. J. O.; Millán, A.; Amaral, V. S.; Palacio, F.; Carlos, L. D. Thermometry at the Nanoscale. *Nanoscale* **2012**, *4*, 4799–4829.

(6) Seppala, J. E.; Migler, K. B. Infrared Thermography of Welding Zones Produced by Polymer Extrusion Additive Manufacturing. *Addit. Manuf.* **2016**, *12*, 71–76.

(7) Seppala, J. E.; Han, S. H.; Hillgartner, K. E.; Davis, C. S.; Migler, K. B. Weld Formation During Material Extrusion Additive Manufacturing. *Soft Matter* **2017**, *13*, 6761–6769.

(8) Bui, T. Q.; Tew, W. L.; Woods, S. I. AC Magnetometry with Active Stabilization and Harmonic Suppression for Magnetic Nanoparticle Spectroscopy and Thermometry. *J. Appl. Phys.* **2020**, *128*, 224901.

(9) Meiklejohn, W. H.; Bean, C. P. New Magnetic Anisotropy. *Phys. Rev.* **1956**, *102*, 1413–1414.

(10) Gangopadhyay, S.; Hadjipanayis, G. C.; Sorensen, C. M.; Klabunde, K. J. Exchange Anisotropy in Oxide Passivated Co Fine Particles. *J. Appl. Phys.* **1993**, *73*, 6964–6966.

(11) Tracy, J. B.; Weiss, D. N.; Dinega, D. P.; Bawendi, M. G. Exchange Biasing and Magnetic Properties of Partially and Fully Oxidized Colloidal Cobalt Nanoparticles. *Phys. Rev. B* **2005**, *72*, No. 064404.

(12) Inderhees, S. E.; Borchers, J. A.; Green, K. S.; Kim, M. S.; Sun, K.; Strycker, G. L.; Aronson, M. C. Manipulating the Magnetic Structure of Co Core/CoO Shell Nanoparticles: Implications for Controlling the Exchange Bias. *Phys. Rev. Lett.* **2008**, *101*, No. 117202.

(13) Feyngenson, M.; Yiu, Y.; Kou, A.; Kim, K.-S.; Aronson, M. C. Controlling the Exchange Bias Field in Co Core/CoO Shell Nanoparticles. *Phys. Rev. B* **2010**, *81*, No. 195445.

(14) Baaziz, W.; Pichon, B. P.; Lefevre, C.; Ulhaq-Bouillet, C.; Greneche, J.-M.; Toumi, M.; Mhiri, T.; Begin-Colin, S. High Exchange Bias in Fe<sub>3</sub>O<sub>4</sub>@CoO Core Shell Nanoparticles Synthesized by a One-Pot Seed-Mediated Growth Method. *J. Phys. Chem. C* **2013**, *117*, 11436.

(15) Xiaojie, L.; Pichon, B. P.; Ulhaq, C.; Lefèvre, C.; Grenèche, J.-M.; Bégin, D.; Bégin-Colin, S. Systematic Study of Exchange Coupling in Core-Shell Fe<sub>3-d</sub>O<sub>4</sub>@CoO Nanoparticles. *Chem. Mater.* **2015**, *27*, 4073–4081.

(16) Dolci, M.; Liu, X.; Leuvre, C.; Derory, A.; Begin, D.; Begin-Colin, S.; Pichon, B. P. Exploring Exchange Bias Coupling in Fe<sub>3-d</sub>O<sub>4</sub>@CoO Core-Shell Nanoparticle 2D Assemblies. *Adv. Funct. Mater.* **2018**, *28*, No. 1706957.

(17) Zhou, L.; Deng, B.; Jiang, Z.; Jiang, Z. Shell Thickness Controlled Core-Shell Fe<sub>3</sub>O<sub>4</sub>@CoO Nanocrystals as Efficient Bifunctional Catalysts for the Oxygen Reduction and Evolution Reactions. *Chem. Commun.* **2019**, *55*, 525.

(18) Flores-Martinez, N.; Franceschin, G.; Gaudisson, T.; Beaunier, P.; Yaacoub, N.; Grenèche, J.-M.; Valenzuela, R.; Ammar, S. Giant Exchange-Bias in Polyol-Made CoFe<sub>2</sub>O<sub>4</sub>-CoO Core-Shell like Nanoparticles. *Part. Part. Syst. Charact.* **2018**, *35*, No. 1800290.

(19) Kavich, D. W.; Dickerson, J. H.; Mahajan, S. V.; Hasan, S. A.; Park, J. H. Exchange Bias of Singly Inverted FeO/Fe<sub>3</sub>O<sub>4</sub> Core-Shell Nanocrystals. *Phys. Rev. B* **2008**, *78*, No. 174414.

(20) Hai, H. T.; Yang, H. T.; Kura, H.; Hasegawa, D.; Ogata, Y.; Takahashi, M.; Ogawa, T. Size Control and Characterization of Wüstite (core)/Spinel (Shell) Nanocubes Obtained by Decomposition of Iron Oleate Complex. *J. Colloid Interface Sci.* **2010**, *346*, 37–42.

(21) Pichon, B. P.; Gerber, O.; Lefevre, C.; Florea, I.; Fleutot, S.; Baaziz, W.; Pauly, M.; Ohlmann, M.; Ulhaq, C.; Ersen, O.; Pierron-Bohnes, V.; Panissod, P.; Drillon, M.; Begin-Colin, S. Microstructural and Magnetic Investigations of Wüstite-Spinel Core-Shell Cubic-Shaped Nanoparticles. *Chem. Mater.* **2011**, *23*, 2886–2900.

(22) Khurshid, H.; Alonso, J.; Nemat, Z.; Phan, M. H.; Mukherjee, P.; Fdez-Gubieda, M. L.; Baranirán, J. M.; Srikanth, H. Anisotropy Effects in Magnetic Hyperthermia: A Comparison Between Spherical and Cubic Exchange-Coupled FeO/Fe<sub>3</sub>O<sub>4</sub> Nanoparticles. *J. Appl. Phys.* **2015**, *117*, No. 17A337.

(23) Salazar-Alvarez, G.; Sort, J.; Surinach, S.; Baro, M. D.; Nogues, J. Synthesis and Size-Dependent Exchange Bias in Inverted Core-Shell MnO/Mn<sub>3</sub>O<sub>4</sub> Nanoparticles. *J. Am. Chem. Soc.* **2007**, *129*, 9102.

- (24) Troitino, N. F.; Murias-Rivas, B.; Rodríguez-González, B.; Salgueirino, V. Exchange Bias Effect in CoO@Fe<sub>3</sub>O<sub>4</sub> Core-Shell Octahedron-Shaped Nanoparticles. *Chem. Mater.* **2014**, *26*, 5566–5575.
- (25) Lima, E.; Winkler, E. L.; Tobia, D.; Troiani, H. E.; Zysler, R. D.; Agostinelli, E.; Fiorani, D. Bimagnetic CoO Core/CoFe<sub>2</sub>O<sub>4</sub> Shell Nanoparticles: Synthesis and Magnetic Properties. *Chem. Mater.* **2012**, *24*, 512–516.
- (26) Antonaropoulos, G.; Vasilakaki, M.; Trohidou, K. N.; Iannotti, V.; Ausanio, G.; Abeykoon, M.; Bozin, E. S.; Lappas, A. Tailoring Defects and Nanocrystal Transformation for Optimal Heating Power in Bimagnetic Co<sub>y</sub>Fe<sub>1-y</sub>O@Co<sub>x</sub>Fe<sub>3-x</sub>O<sub>4</sub> Particles. *Nanoscale* **2022**, *14*, 382–401.
- (27) Lavorato, G. C.; Saleta, M. E.; Figueroa, S. J. A.; Tobia, D.; Mauricio, J. C.; Lohr, J.; Baggio-Saitovitch, E.; Troiani, H. E.; Zysler, R. D.; Lima, E.; Winkler, E. L. Cation Occupancy in Bimagnetic CoO-core/Co<sub>1-x</sub>Zn<sub>x</sub>Fe<sub>2</sub>O<sub>4</sub>-Shell (x = 0-1) Nanoparticles. *J. Alloys Compd.* **2021**, *877*, No. 160172.
- (28) Anderson, N. R.; Camley, R. E. Temperature-Dependent Magnetization in Bimagnetic Nanoparticles with Antiferromagnetic Interfacial Exchange. *Phys. Rev. B* **2016**, *94*, No. 134432.
- (29) Jubb, A. M.; Allen, H. C. Vibrational Spectroscopic Characterization of Hematite, Maghemite, and Magnetite Thin Films Produced by Vapor Deposition. *ACS Appl. Mater. Interfaces* **2010**, *2*, 2804–2812.
- (30) Chamrinski, I.; Burns, G. Infrared- and Raman-Active Phonons of Magnetite, and Maghemite, and Hematite: A Computer Simulation and Spectroscopic Study. *J. Phys. Chem. B* **2005**, *109*, 4965–4968.
- (31) Giellisse, P. J.; Plendl, J. N.; Mansur, L. C.; Marshall, R.; Mitra, S. S.; Mykolajewycz, R.; Smakula, A. J. Infrared Properties of NiO and CoO and Their Mixed Crystals. *J. Appl. Phys.* **1965**, *36*, 2446.
- (32) Kant, C.; Rudolf, T.; Schrettle, F.; Mayr, F.; Deisenhofer, J.; Lunkenheimer, P.; Eremin, M. V.; Loidl, A. Optical Spectroscopy in CoO: Phononic, Electric, and Magnetic Excitation Spectrum within the Charge-Transfer Gap. *Phys. Rev. B* **2008**, *78*, No. 245103.
- (33) Murias-Rivas, B.; Salgueirino, V. Thermodynamic CoO-Co<sub>3</sub>O<sub>4</sub> Crossover using Raman Spectroscopy in Magnetic Octahedron-Shaped Nanocrystals. *J. Raman Spectrosc.* **2017**, *48*, 837–841.
- (34) Baaziz, W.; Pichon, B. P.; Fleutot, S.; Liu, Y.; Lefevre, C.; Greneche, J.-M.; Toumi, M.; Mhiri, T.; Begin-Colin, S. Magnetic Iron Oxide Nanoparticles: Reproducible Tuning of the Size and Nano-sized-Dependent Composition, Defects, and Spin Canting. *J. Phys. Chem. C* **2014**, *118*, 3795–3810.
- (35) Dehsari, H. S.; Ksenofontov, V.; Moller, A.; Jakob, G.; Asadi, K. Determining Magnetite/Maghemite Composition and Core-Shell Nanostructure from Magnetization Curve for Iron Oxide Nanoparticles. *J. Phys. Chem. C* **2018**, *122*, 28292–28301.
- (36) Yadav, T. S.; et al. Impact of Grain Size and Structural Changes on Magnetic, Dielectric, Electrical Impedance and Modulus Spectroscopic Characteristics of CoFe<sub>2</sub>O<sub>4</sub> Nanoparticles Synthesized by Honey Mediated sol-gel Combustion Method. *Adv. Nat. Sci.: Nanosci. Nanotechnol.* **2017**, *8*, No. 045002.
- (37) Kampermann, L.; Klein, J.; Korte, J.; Kowollik, O.; Pflingsten, O.; Smola, T.; Saddeler, S.; Piotrowiak, T. H.; Salamon, S.; Landers, J.; Wende, H.; Ludwig, A.; Schulz, S.; Bacher, G. Link between Structural and Optical Properties of Co<sub>x</sub>Fe<sub>3-x</sub>O<sub>4</sub> Nanoparticles and Thin Films with Different Co/Fe Ratios. *J. Phys. Chem. C* **2021**, *125*, 14356–14365.
- (38) Shi, H.; He, X. Large-scale Synthesis and Magnetic Properties of Cubic CoO Nanoparticles. *J. Phys. Chem. Solids* **2012**, *73*, 646–650.
- (39) Oles, S. D.; Courts, S. S. Resolution and Accuracy of Cryogenic Temperature Measurements. In *Temperature: Its Measurement and Control in Science and Industry*; Springer, 1992; Vol. 6, pp 1225–1230.
- (40) Dann, J. R. A.; Verpoort, P. C.; Ferreira de Oliveira, J.; Rowley, S. E.; Datta, A.; Kar-Narayan, S.; Ford, C. J. B.; Conduit, G. J.; Narayan, V. Au-Ge Alloys for Wide-Range Low-Temperature On-Chip Thermometry. *Phys. Rev. Appl.* **2019**, *12*, No. 034024.
- (41) Rus, E. D.; Correa, E. L.; Groopman, E.; Williamson, T.; Hijazi, H.; Kasaei, L.; Dennis, C. L.; Moffat, T. P. Magnetic Characterization of Electrodeposited Pt<sub>1-x</sub>Ni<sub>x</sub> Alloy Films: Influence of Deposition Potential and Presence of Boric Acid. *J. Electrochem. Soc.* **2022**, *169*, No. 092518.
- (42) Sun, S.; Zeng, H.; Robinson, D. B.; Raoux, S.; Rice, P. M.; Rice, P. M.; Wang, S. X.; Wang, S. X.; Li, G. Monodisperse MFe<sub>2</sub>O<sub>4</sub> (M = Fe, Co, Mn) Nanoparticles. *J. Am. Chem. Soc.* **2004**, *126*, 273–279.
- (43) Xu, Z.; Shen, C.; Hou, Y.; Gao, H.; Sun, S. Oleylamine as Both Reducing Agent and Stabilizer in a Facile Synthesis of Magnetite Nanoparticles. *Chem. Mater.* **2009**, *21*, 1778–1780.
- (44) Pourmiri, S.; Tzitzios, V.; Hadjipanayis, G. C.; Meneses Brassea, B. P.; El-Gendy, A. A. Magnetic Properties and Hyperthermia Behavior of Iron Oxide Nanoparticle Clusters. *AIP Adv.* **2019**, *9*, No. 125033.